

Discovery of multi-phase cold accretion in a massive galaxy at $z=0.7$

Glenn G. Kacprzak,^{1,2*} Christopher W. Churchill,^{3,4} Charles C. Steidel,⁵
 Lee R. Spitler,¹ and Jon A. Holtzman,³

¹ Centre for Astrophysics and Supercomputing, Swinburne University of Technology, PO Box 218, Victoria 3122, Australia

² Australian Research Council Super Science Fellow

³ Department of Astronomy, New Mexico State University, Las Cruces, NM 88003

⁴ Visiting Professor, Swinburne University of Technology, Victoria 3122, Australia

⁵ California Institute of Technology, MS 105-24, Pasadena, CA 91125, USA

Accepted August 16 2012

ABSTRACT

We present detailed photo+collisional ionization models and kinematic models of the multi-phase absorbing gas, detected within the *HST*/COS, *HST*/STIS, and Keck/HIRES spectra of the background quasar TON 153, at 104 kpc along the projected minor axis of a star-forming spiral galaxy ($z = 0.6610$). Complementary $g'r'i'Ks$ photometry and stellar population models indicate that the host galaxy is dominated by a ~ 4 Gyr stellar population with slightly greater than solar metallicity and has an estimated $\log M_* = 11$ and a $\log M_{\text{vir}} = 13$. Photoionization models of the low ionization absorption, (Mg I, Si II, Mg II and C III) which trace the bulk of the hydrogen, constrain the multi-component gas to be cold ($\log T = 3.8 - 5.2$) and metal poor ($-1.68 \leq [X/H] \leq -1.64$). A lagging halo model reproduces the low ionization absorption kinematics, suggesting gas coupled to the disk angular momentum, consistent with cold accretion mode material in simulations. The C IV and O VI absorption is best modeled in a separate collisionally ionized metal-poor ($-2.50 \leq [X/H] \leq -1.93$) warm phase with $\log T = 5.3$. Although their kinematics are consistent with a wind model, given the 2 – 2.5 dex difference between the galaxy stellar metallicity and the absorption metallicity indicates the gas cannot arise from galactic winds. We discuss and conclude that although the quasar sightline passes along the galaxy minor axis at projected distance of 0.3 virial radii, well inside its virial shock radius, the combination of the relative kinematics, temperatures, and relative metallicities indicated that the multi-phase absorbing gas arises from cold accretion around this massive galaxy. Our results appear to contradict recent interpretations that absorption probing the projected minor axis of a galaxy is sampling winds.

Key words: —galaxies: ISM, haloes —quasars: absorption lines.

1 INTRODUCTION

Over the last decade, simulations have shown that galaxy evolution is highly dependent on gas accretion occurring via two modes: hot and cold accretion. Current cosmological simulations demonstrate that the majority of gas accreted at early epochs onto galaxies occurs via the cold mode, which has temperatures of $T \sim 10^4 - 10^5$ K and metallicities of $Z \lesssim 0.01Z_\odot$. Cold-mode gas is preferentially accreted along cosmic filaments/streams and have high densities and low cooling times providing a large supply of gas penetrating through hot halos surrounding galaxies (Kereš et al. 2005; Dekel & Birnboim 2006; Ocvirk et al. 2008; Kereš et al. 2009; Brooks et al. 2009; Dekel et al. 2009; Ceverino et al. 2010; Stewart et al. 2011a,b; van de Voort et al. 2011; van de Voort & Schaye 2011; Faucher-Giguère et al. 2011).

It is expected that cold accretion should comprise no more than 7% of the total H I mass density at $z \sim 1$ (Kacprzak & Churchill 2011).

It is further expected that cold accretion truncates when the host galaxy mass exceeds $\sim 10^{12} M_\odot$, since infalling gas becomes shock heated to the halo virial temperature ($\sim 10^6$) and is predicted to dramatically reduce the cold accretion cross-section to a tiny fraction (e.g., Dekel & Birnboim 2006; Kereš et al. 2005; Ocvirk et al. 2008; Dekel et al. 2009; Kereš et al. 2009; Stewart et al. 2011a; Brooks et al. 2009; van de Voort et al. 2011; van de Voort & Schaye 2011) of the observed halo gas cross-section (Kacprzak et al. 2008; Chen et al. 2010). However, it is expected that these dense filaments can still survive within hot halos and could provide an efficient means of feeding massive galaxies with pristine gas (e.g., Kereš et al. 2005).

The study of absorbing foreground gas detected in background quasar spectra allows us to probe these otherwise unob-

* gkacprzak@astro.swin.edu.au

servable comic filaments and outflows. MgII absorption is ideal for detecting cold mode and hot mode accretion, wind outflows, etc., since it probes gas with a large range of neutral hydrogen column densities, $10^{16} \lesssim N(\text{H I}) \lesssim 10^{22} \text{ cm}^{-2}$ (Churchill et al. 2000a; Rigby, Charlton, & Churchill 2002) with gas temperature of around 30,000–40,000 K and average total hydrogen densities of $\sim 0.1 \text{ atoms cm}^{-3}$ (Churchill, Vogt, & Charlton 2001; Ding, Charlton, & Churchill 2005). It has also been thoroughly demonstrated that MgII absorption is produced within gaseous halos surrounding galaxies and is not produced within the intergalactic medium (IGM) (see Churchill, Kacprzak, & Steidel 2005).

Over the last decade, strong MgII absorption has also been observed to directly trace 100–1000 km s^{-1} galactic-scale outflows (Tremonti et al. 2007; Weiner et al. 2009; Martin & Bouché 2009; Rubin et al. 2010; Coil et al. 2011; Martin et al. 2012) that extend out to at least 50 kpc along the galaxy minor axis (Bordoloi et al. 2011; Bouché et al. 2011; Kacprzak et al. 2012). Galactic winds have been observed over a large range of redshifts and detected using a range of ions (see Steidel et al. 2010, and references therein). Correlations between galaxy colors and star formation rates with MgII equivalent widths also indirectly suggest that absorption is produced in outflows (Zibetti et al. 2007; Noterdaeme et al. 2010; Nestor et al. 2011).

However, MgII has been observed infalling (Martin et al. 2012) into highly inclined galaxies with velocities of 100–200 km s^{-1} (Rubin et al. 2011). This is consistent with Kacprzak et al. (2011b) who showed that absorption strength is correlated with the orientation of the galaxy major axis, implying that a significant fraction of weaker MgII absorption systems are likely accreting toward the galaxy via cold flows. The bimodal azimuthal angle distribution of quasar sight-lines around MgII absorption selected galaxies also suggests that infall occurs along the projected galaxy major axis (Bouché et al. 2011; Kacprzak et al. 2012). These cold-flow streams likely produce a circumgalactic co-rotating gas component that is predominately infalling towards the galaxy and, in absorption, these structures are expected to have $\sim 100 \text{ km s}^{-1}$ velocity offsets relative to the host galaxy *and* in the same direction of galaxy rotation (Stewart et al. 2011b). These models are consistent with previous observations of Steidel et al. (2002) and Kacprzak et al. (2010a) that show MgII absorption residing fully to one side of the galaxy systemic velocity and usually aligned with expected galaxy rotation direction, with the absorption essentially mimicking the extension of the galaxy rotation curve out into the halo. We expect low ionization states, such as MgI, MgII, SiII, CII and CIII to be ideal for tracing cold mode accretion given metallicity, temperatures and densities expected.

A reliable means of determining the origins of the absorbing gas is to obtain both the host-galaxy and absorption-line metallicity. Absorption-line metallicities for a handful of systems have been determined to range between $[\text{M}/\text{H}] < -1.8$ to -1 while existing near sub- L^* galaxies that have nearly solar metallicities (Zonak et al. 2004; Chen et al. 2005; Tripp et al. 2005; Cooksey et al. 2008; Kacprzak et al. 2010b; Ribaud et al. 2011; Thom et al. 2011). It is postulated that these extremely low metallicity absorption systems are likely accreting onto their host galaxies and possibly trace cold mode accretion, which is still expected for these sub- L^* galaxies. In the rare case where absorption-line metallicities are larger than the host galaxy is suggestive that the absorption is probing winds (Péroux et al. 2011).

Here we target a particular galaxy that has MgII absorption consistent with disk-like kinematics, possibly tracing cold accre-

tion. The absorption also contains a separate warm phase as indicated by separate strong CIV absorption that does not coincide with MgII. We have obtained supplementary *HST*/COS data in order to determine the physical properties of the gas. In this paper, we perform kinematic and photo+collisional ionization models of multi-phase absorbing gas obtained from *HST*/COS, *HST*/STIS, and Keck/HIRES, which is associated with star-forming spiral galaxy at $z = 0.6610$. In § 2 we describe our targeted galaxy and our data. We discuss our absorption-line analysis in § 3. In § 4 we describe the host galaxy properties determined from broad-band photometry and stellar population models. In § 5 we describe the results of our kinematics and photo+collisional ionization models and the physical properties of the absorbing gas. In § 6, we discuss the possible origins of the absorption and our concluding remarks are in § 7. Throughout we adopt an $H_0 = 70 \text{ km s}^{-1} \text{ Mpc}^{-1}$, $\Omega_M = 0.3$, $\Omega_\Lambda = 0.7$ cosmology.

2 TARGET FIELD AND OBSERVATIONS

TON 153, also known as Q1317+227, is a bright ($V=16.0$ mag) quasar at $z_{em} = 1.017$. Inspection of a low resolution quasar spectrum revealed two MgII absorption systems at $z_{abs} = 0.29$ and $z_{abs} = 0.66$ (Steidel & Sargent 1992). Following a spectroscopic survey of galaxies in close angular proximity to the quasar sight-line, Steidel et al. (2002) discovered galaxies G1 and G2 shown in Figure 1. The quiescent early-type galaxy G1 has a redshift of $z_{gal} = 0.6719$ and the star-forming disk galaxy G2 has a redshift of $z_{gal} = 0.6610$. Churchill et al. (2007) demonstrated that G1 was associated with a Ly α complex that did not have any observable metals even though it resides at $D = 58.1$ kpc; well within the 100 kpc where metals are expected (e.g., Chen et al. 2001; Kacprzak et al. 2008; Chen et al. 2010; Tumlinson et al. 2011). In a companion paper (Churchill et al. 2012b), we further discuss G1 and its associated absorption lines. The galaxy G2 is at $D = 103.9$ kpc and is associated with extensive metal-line/LLS absorption at $z_{abs} = 0.6601$ (Steidel & Sargent 1992; Bahcall et al. 1993, 1996; Churchill et al. 2000a; Ding, Charlton, & Churchill 2005; Churchill et al. 2007) and is the focus of this paper.

2.1 HST Imaging

In Figure 1 we present a 4700 second *HST*/WFPC–2 F702W image (PID 5984; PI Steidel) that was reduced using the WFPC-2 Associations Science Products Pipeline (WASPP¹). Note that the F702W filter provides a bandpass similar to a rest-frame Johnson B-band filter for galaxies at $z \sim 0.6$. Galaxy magnitudes and luminosities were obtained from Churchill et al. (2012a) and are based on the AB system. The GIM2D software (Simard et al. 2002) was used to obtain quantified galaxy morphological parameters that were published in Kacprzak et al. (2011b) and Churchill et al. (2012a).

2.2 Ground-based Imaging

To further constrain the properties of G2, we analyzed multi-band $g'r'i'$ and Ks imaging. The $g'r'i'$ -bands were obtained using SPIcam CCD imager on the APO 3.5 m telescope. SPIcam has a field of view of $4.78 \times 4.78'$ and a spatial resolution of $0.14''/\text{pixel}$. Our

¹ <http://archive.stsci.edu/hst/wfpc2/pipeline.html>

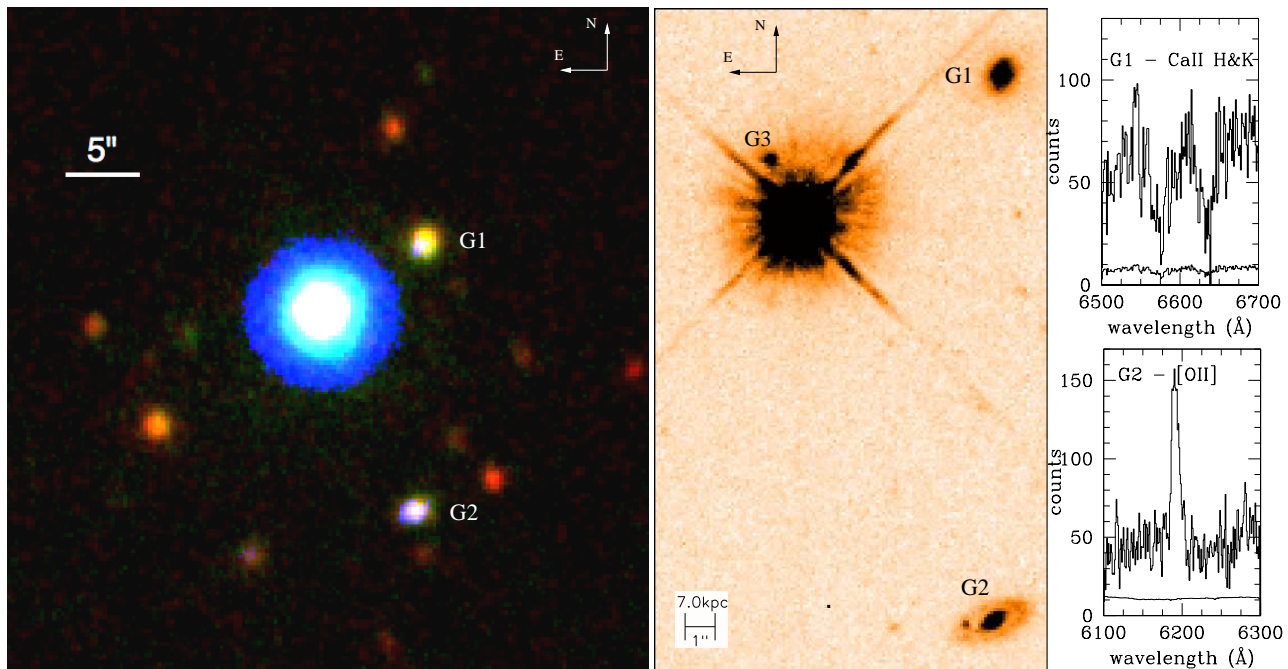


Figure 1. — (left) Ground-based g' - (blue), i' - (green) and Ks - band (red) color composite centered on the quasar. Note that G1 is redder than G2 (see Churchill et al. 2012b). Also note that the surrounding galaxies in the field are extremely red compared to both $z \sim 0.6$ galaxies, indicating that they are at much higher redshifts and not associated with the absorption. (middle) A $13'' \times 22''$ *HST*/WFPC-2 F702W image of the quasar field TON 153. The quasar is the brightest object in the northeast corner of the image. G2 is associated with a variety of metal-lines shown in Figure 2. A possible object seen within $\sim 1''$ northeast of the quasar (G3) has not been successfully identified spectroscopically since the quasar is bright. Note the quasar sight-line passes near the minor axis of the moderately inclined disk of G2. — (top right) A Keck/LRIS spectrum of G1 containing Ca II H & K confirms the redshift of G1 to be $z_{gal} = 0.6719$. — (bottom left) A Keck/LRIS spectrum of G2 containing [O II] emission confirms the redshift of G2 to be $z_{gal} = 0.6610$.

observations were taken with on-chip binning of 2×2 which provides a plate scale of $0.28''/\text{pixel}$. The images were taken as part of a large survey program and were observed over 4 nights between March 2006 and March 2007 providing total exposure times in the $g'r'i'$ of 5190, 4630 and 4350 seconds, respectively, with typical seeing of $1.1 - 1.6''$.

Multiple frames were taken in each filter and each frame was individually reduced using standard IDL and IRAF² packages. Pixel-to-pixel variations were removed using a combination of dome and twilight sky flat fields. Due to PSF/seeing variations over the long exposures, cosmic rays were removed from each frame separately. The SPIcam pixels are sufficiently small that interpolation errors do not lead to significant photometric uncertainties. The astrometry was calibrated by matching field stars from each frame to USNO A2.0 catalog stars.

The photometric zeropoints were established using a number of stars from the SDSS catalog. Since the APO $g'r'i'$ filter/detector combination does not exactly match that of the SDSS survey, there can exist color terms between the two systems. We derived these color terms by analyzing the SDSS stellar photometry from over 30 fields and produced a single photometric solution. We adopt the color term derived from the large set of observations and the average corrections are of the order of 0.1 magnitudes.

Deep near-infrared (Ks) band images were obtained in 1994

February 24 using the Kitt Peak 4-m Mayall telescope and the IRIM NICMOS 3 256×256 camera with $0.6''/\text{pixel}$. These images were part of a more extensive Mg II galaxy survey of Steidel, Dickinson, & Persson (1994). The images were reduced using the contributed IRAF package DIMSUM³. The photometric zeropoints were established using a number of stars from the 2MASS point-source catalog (Skrutskie et al. 2006).

In Figure 1 we present a $g'i'Ks$ color composite image centered on TON 153 with galaxies G1 and G2 labeled. See companion paper Churchill et al. (2012b) for further discussions of the properties of G1. Note that all other objects near the quasar sight-line are red compared to the two $z \sim 0.65$ galaxies, indicating that all the other objects are likely at much higher redshifts and that G1 and G2 are likely isolated objects. Churchill et al. (2012b) noted that the ROSAT X-ray luminosity limit for this field is four orders of magnitude less than what is expected for cluster centers and is consistent with the expected luminosity for early-type galaxy halos at $z = 0.67$. In addition, the absorption metallicities determined by Churchill et al. (2012b) for G1, and those found here, are 1–2dex lower than expected for inter-cluster medium. Thus, it is likely that the absorption does not arise in a cluster environment.

The galaxy G3 is located within $\sim 1''$ northeast of the quasar sight-line and has not been successfully identified spectroscopically since the quasar is bright. It is possible that this object is responsible for either the absorption associated with G1, G2, the $z = 0.29$ absorption system, absorption at the quasar redshift, or

² IRAF is written and supported by the IRAF programming group at the National Optical Astronomy Observatories (NOAO) in Tucson, Arizona. NOAO is operated by the Association of Universities for Research in Astronomy (AURA), Inc. under cooperative agreement with the National Science Foundation.

³ <http://iraf.noao.edu/iraf/ftp/contrib/dimsumV3/>. DIMSUM was contributed by P. Eisenhardt, M. Dickinson, S. A. Stanford, & F. Valdez.

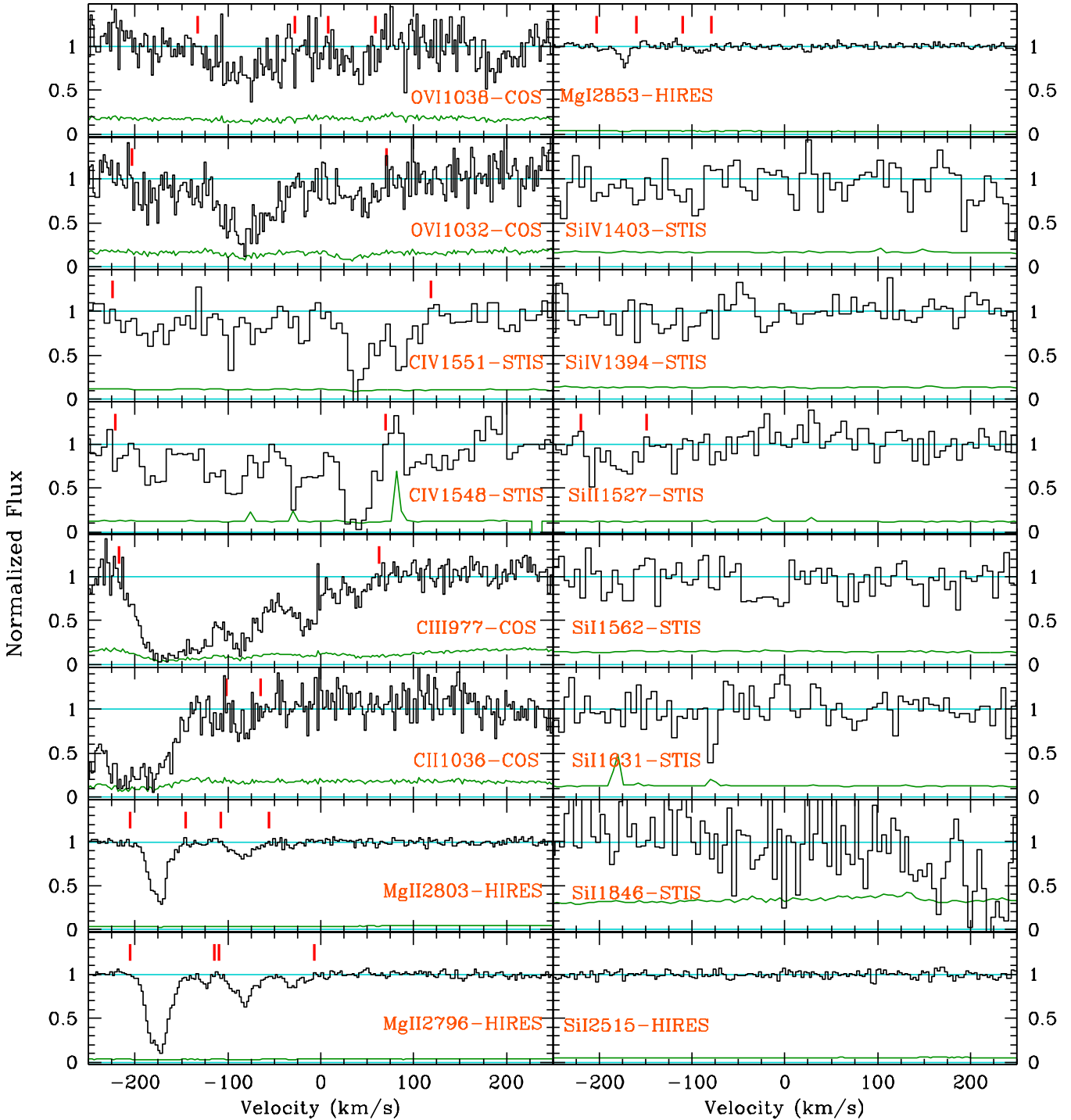


Figure 2. — Metal absorption-lines associated with the $z = 0.6610$ galaxy G2 obtained from *HST*/COS, *HST*/STIS and Keck/HIRES. In each panel the transition and instrument are labeled. The absorption-line data (black) are relative to the systemic velocity of G2. The regions highlighted by the tick-marks (red) indicate the detected absorption features and the location of the tick-marks are defined to be where the equivalent width per resolution element recovers to a 1σ detection threshold. The sigma spectrum is shown below the data (green).

other metal-lines identified in this sight-line. If G3 is at $z = 0.67$, than Churchill et al. (2012b) estimates its mass to be a factor of ten less than the mass of G2 and would have a similar metallicity to G2 according to mass-gas metallicity relations (e.g., Savaglio et al. 2005). Thus, if G3 is at the same redshift of G2, it could be consid-

ered as a satellite of G2 and would occupy the same gaseous and dark matter halo.

Photometry for calibration and science was extracted using SExtractor (Bertin & Arnouts 1996) using the MAGAUTO measurements. Corrections for Galactic dust extinction were applied to the galaxies using the dust maps of Schlegel et al. (1998). We ob-

tained final dust-, color- and seeing-corrected AB magnitudes for G1 of $m_{g'} = 23.43 \pm 0.03$, $m_{r'} = 22.17 \pm 0.03$, $m_{i'} = 21.01 \pm 0.03$ and $m_{Ks'} = 19.4 \pm 0.1$ (Churchill et al. 2012b) and for G2 of $m_{g'} = 23.23 \pm 0.03$, $m_{r'} = 22.32 \pm 0.03$, $m_{i'} = 21.41 \pm 0.03$ and $m_{Ks'} = 19.9 \pm 0.1$.

2.3 Galaxy Spectroscopy

The galaxies shown in Figure 1 were spectroscopically identified by Steidel et al. (2002) and their spectra were first presented in Churchill et al. (2007). A possible object seen within $\sim 1''$ from the quasar seen in the image has not been successfully identified spectroscopically since the quasar is bright. The details of the Keck/LRIS spectroscopic observations can be found in Steidel et al. (2002) and Churchill et al. (2007); Churchill et al. (2012b). The spectra are both vacuum and heliocentric velocity corrected. Galaxy G1, identified by Ca II H & K absorption yields a $z_{gal} = 0.6719$, is associated with broad Ly α complex that spans 1400 km s^{-1} and yet contains only very weak metals lines (Churchill et al. 2007; Churchill et al. 2012b). Galaxy G2 was identified by a [O II] emission line, placing it at $z_{gal} = 0.6610$. This galaxy is associated with extensive metal-line/LLS absorption at $z_{abs} = 0.6601$ (Bahcall et al. 1993, 1996; Churchill et al. 2000a; Ding, Charlton, & Churchill 2005; Churchill et al. 2007) and is the focus of this paper. We discuss G2's associated metals-lines in the next sections.

2.4 Quasar Spectroscopy

Some of the $z_{abs} = 0.6601$ absorption properties were measured from a 3600 second Keck/HIRES ($R \sim 45,000$) exposure observed in 1995 January. The details of the observation and data reduction are described in Churchill & Vogt (2001). In addition, a 12,000 second *HST*/STIS E230M ($R \sim 30,000$) exposure was obtained (PID 8672; PI Churchill) and the data reduction details are found in Ding, Charlton, & Churchill (2005).

Recent *HST*/COS observations of the quasar ($R \sim 18,000$) were obtained using the FUV G160M grating and the NUV G185M grating (PID 11667; PI Churchill). The FUV observations were centered at 1600 \AA and took place on 25 June 2010 with an exposure time of 12,580 seconds. The NUV observations consisted of two exposures that occurred on 26 May 2010 and were optimally co-added. The first 5420 second NUV exposure was centered at 1921 \AA and the 4970 second NUV exposure was centered at 1941 \AA . The COS spectra were reduced using the standard *HST* IRAF pipeline. All spectra are both vacuum and heliocentric velocity corrected.

It is important to note that the wavelength solutions across these multiple instruments are consistent at the sub-pixel level. This was verified across all spectrographs by centroiding common ionization absorption lines from the data presented here and the data from Churchill et al. (2012b).

Analysis of the absorption profiles was performed using interactive software (see Churchill et al. 1999, 2000a; Churchill & Vogt 2001) for local continuum fitting, objective feature identification, and measuring absorption properties. Velocity widths and equivalent widths of the absorption systems are measured between the pixels where the equivalent width per resolution element recovers to the 1σ detection threshold (Churchill et al. 1999).

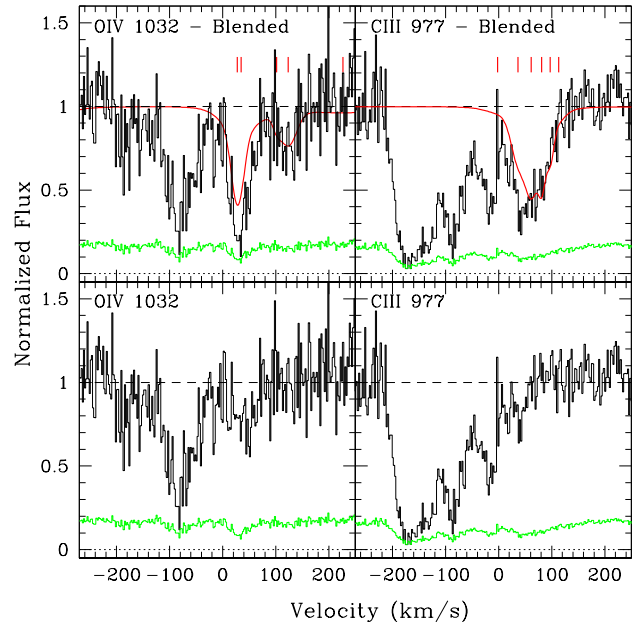


Figure 3. — (top-left) COS/HST O VI $\lambda 1032$ transition associated with G2 is blended with Ly β from the $z = 0.67$ G1 Ly α complex (Churchill et al. 2007; Churchill et al. 2012b). The Ly β fit (red) was constrained by simultaneous Voigt profile fits to the Ly α , Ly γ , Ly ϵ , and Ly ζ . — (top-right) COS/HST C III $\lambda 977$ transition associated with G2 is blended with a Ly γ from the $z = 0.67$ G1 Ly α complex (Churchill et al. 2007; Churchill et al. 2012b). The Voigt profile fit was constrained by the Ly α , Ly β , Ly ϵ , and Ly ζ which produce the Ly γ fit shown (red). — (bottom-left) The deblended O VI $\lambda 1032$ line associated with G2. — (bottom-right) The deblended C III $\lambda 977$ line associated with G2.

3 QUASAR ABSORPTION-LINE ANALYSIS

In Figure 2 we present the absorption-line data and in Table 1 we present the measured equivalent widths and column densities. We discuss below how the column densities and/or limits were computed for each transition. We further discuss how we account for higher redshift hydrogen-line blends that contaminate the O VI $\lambda 1032$ and C III $\lambda 977$ transitions (see Figure 3).

The H I column density was adopted from Churchill et al. (2007), obtained by simultaneously fitting the Ly α , Ly β , and Lyman break obtained from a FOS spectrum, was determined to be $\log[N(\text{H I})] = 18.3 \pm 0.3$. This is consistent with the results of Rao et al. (2006), who fit only the Ly α line, and determined the column density to be 18.57 ± 0.02 . If we were to use the Rao et al value, our derived metallicities would decrease by 0.27 dex.

We also note upon analyzing the C IV $\lambda \lambda 1548, 1550$ doublet, we have deemed the reddest component seen in the C IV $\lambda 1551$ transition, at roughly 80 km s^{-1} , to be real and has been included in our analysis. This feature does not appear in the C IV $\lambda 1548$ line since this region is contaminated by poor sky subtraction. This component was omitted by the analysis of Ding, Charlton, & Churchill (2005) but included here.

3.1 Accounting for Blends in O VI $\lambda 1032$ and C III $\lambda 977$

Churchill et al. (2012b) performed detailed Voigt profile (VP) fits to the Lyman series, using the *HST*/COS spectra, in order to determine the gas-phase properties of the G1 absorption complex.

Table 1. Absorption Properties^a

Ion	Instrument/ Telescope	W_r (Å)	$\log N(X)$	W_r^{blue} (Å) ^b	${}^b\log N(X)^{blue}$	W_r^{red} (Å) ^b	${}^b\log N(X)^{red}$
Mg II $\lambda 2796$	HIRES/Keck	0.348±0.007		0.348±0.007		<0.0049	
Mg II $\lambda 2803$	HIRES/Keck	0.198±0.006		0.198±0.006		<0.0060	
MgII			13.11 ^{+0.07} _{-0.07}		13.11 ^{+0.07} _{-0.07}		≤11.06
Mg I $\lambda 2853$	HIRES/Keck	0.039±0.005		0.039±0.005		<0.0049	
MgI			11.54 ^{+0.06} _{-0.05}		11.54 ^{+0.05} _{-0.05}		≤10.58
Si I $\lambda 2515$	HIRES/Keck	<0.0066		<0.0066		<0.0066	
Si I $\lambda 1846$	STIS/HST	<0.053		<0.053		<0.053	
Si I $\lambda 1631$	STIS/HST	<0.019		<0.019		<0.019	
Si I $\lambda 1562$	STIS/HST	<0.023		<0.023		<0.023	
SiI			≤11.8		≤11.8		≤11.8
Si II $\lambda 1527$	STIS/HST	0.067±0.013		0.067±0.013		<0.018	
SiII			13.16 ^{+0.11} _{-0.08}		13.16 ^{+0.11} _{-0.08}		≤12.6
Si IV $\lambda 1394$	STIS/HST	<0.019		<0.019		<0.019	
Si IV $\lambda 1403$	STIS/HST	<0.023		<0.023		<0.023	
SiIV			≤12.4		≤12.4		≤12.4
C II $\lambda 1036$	COS/HST	>0.018±0.005 ^c		>0.018±0.005 ^c		<0.012	
CII			> 13.39 ^{+0.09} _{-0.07}		> 13.39 ^{+0.09} _{-0.07}		≤13.1
C III $\lambda 977$	COS/HST	0.467±0.008		0.431±0.007		0.036±0.004	
CIII			14.20 ^{+0.03} _{-0.02}		14.18 ^{+0.03} _{-0.03}		12.88 ^{+0.05} _{-0.05}
C IV $\lambda 1548$	STIS/HST	>0.508±0.027 ^d		0.315±0.024		>0.193±0.031 ^d	
C IV $\lambda 1551$	STIS/HST	0.417±0.026		0.189±0.021		0.228±0.018	
CIV			14.41 ^{+0.06} _{-0.05}		14.11 ^{+0.07} _{-0.05}		14.15 ^{+0.08} _{-0.07}
O VI $\lambda 1032$	COS/HST	0.233±0.012		0.189±0.011		0.044±0.006	
O VI $\lambda 1038$	COS/HST	0.105±0.010		0.076±0.008		0.029±0.007	
OVI			14.49 ^{+0.03} _{-0.03}		14.33 ^{+0.04} _{-0.04}		13.94 ^{+0.07} _{-0.06}
HI	FOS/HST COS/HST		18.3±0.3 ^e		18.3±0.3 ^e		16.03 ^{+0.18} _{-0.18}

^a The equivalent width limits are computed at the 3σ -level and are for an unresolved cloud. The column densities are measured using the AOD method and the column density limits are computed using the COG analysis (see text).

^b W_r and $\log N(X)$ are quoted for absorption blueward (W_r^{blue}) redward (W_r^{red}) of the galaxy systemic velocity. The velocity windows used to compute $\log N(X)$ are $-240 \leq v_{abs} \leq -3 \text{ km s}^{-1}$ for gas blueward of the G2 systemic velocity and $-3 \leq v_{abs} \leq 220 \text{ km s}^{-1}$ for gas redward of the G2 systemic velocity.

^c C II is blended with an unknown line at $v_{abs} < -100 \text{ km s}^{-1}$, which is why the C II is expressed as a lower limit. The exact value quoted is valid over the velocity window shown in Figure 2.

^d C IV $\lambda 1551$ is affected by poor sky subtraction and is expressed as a lower limit. The exact value quoted is valid over the velocity window shown in Figure 2.

^e The H I column density is adopted from Churchill et al. (2007) and was determined by simultaneously fitting the Ly α , Ly β , and the Lyman limit absorption.

The VP fits were performed using our own software MINFIT (Churchill & Vogt 2001; Churchill, Vogt, & Charlton 2001). The HST/COS instrumental line spread functions for the spectrograph settings, and also for the observed wavelength of each modeled transition, was computed by interpolating the on-line tabulated data (Dixon et al. 2010; Kriss 2011).

Churchill et al. (2012b) determined that a portion of the G1 Ly β complex was blended with the O VI $\lambda 1032$ associated with G2, while a different portion of the G1 Ly γ complex was blended with C III $\lambda 977$ associated with G2 as shown in Figure 3 (the full Ly β and Ly γ complex is not shown since it spans roughly 1400 km s^{-1}).

The VP fits of the O VI $\lambda 1032$ blended portion of the Ly β complex was well constrained by the non-blended Ly α , Ly γ , Ly ϵ , and Ly ζ lines. The VP fits of the C III $\lambda 977$ blended portion of the Ly γ complex was well constrained by the non-blended Ly α , Ly β , Ly ϵ , and Ly ζ lines. We show the blended and deblended O VI $\lambda 1032$ and C III $\lambda 977$ lines in Figure 3. Given that G1s hydrogen lines are unsaturated and can be well modeled using most of the H I series, we are confident that we have a robust correction for the spectral shape

of the O VI $\lambda 1032$ and C III $\lambda 977$ lines. Furthermore, these corrections only effect regions redward of the galaxy systemic velocity.

3.2 Apparent Optical Depth Method

We employed the apparent optical depth method (AOD) to measure the column densities for each transition using the formalism of Savage & Sembach (1991) and Churchill & Vogt (2001). In the cases that multiple transitions of a given ion were measured, we computed the optimal weighted mean column density in each velocity bin. Since the weighted mean requires the inverse square of the uncertainties, in these cases we treated the non-normal distributions in the uncertainties of the optical depths using the quadratic model of D'Agostini (2000); D'Agostini & Raso (2000); Barlow (2003). The quadratic model approximates the probability distribution of the asymmetric uncertainties in each optical depth data point by a parabola fit to the dimidated Gaussian constructed from the upward and downward measured optical depth uncertainties. Relative to a treatment that neglects the non-normal distribution in the

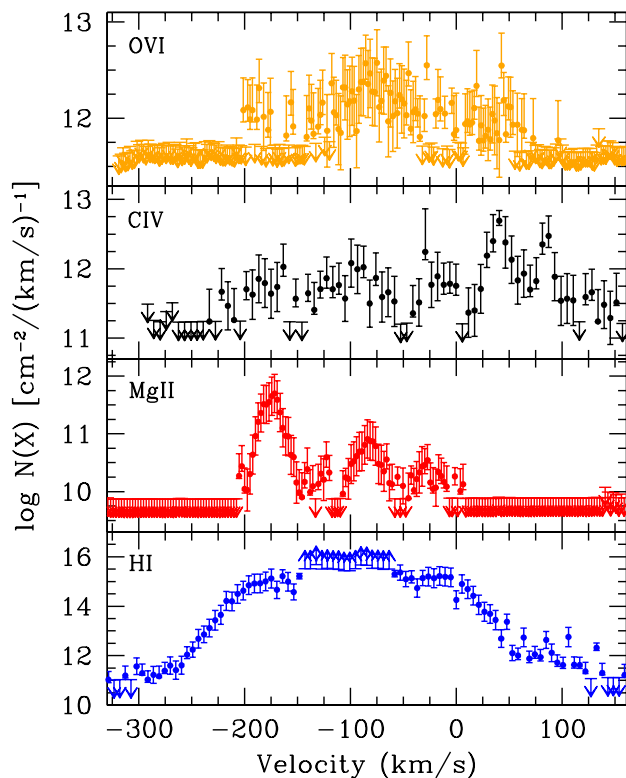


Figure 4. — The doublet optimally combined apparent optical depth distribution for OVI (orange), CIV (black) and MgII (red). The H_I (blue) optical depth distribution was produced by combining the entire Lyman series. The total column densities are integrated over the velocity bins. Note that the H_I is still saturated in the center of the profile. Also note the velocity structure difference between the profiles and that the majority of the hydrogen is at velocities consistent with the MgII whereas the majority of the CIV has velocities consistent with a small fraction of the total H_I.

uncertainties, the method effectively provides a point-by-point bias correction to the resulting mean.

In Figure 4 we present the optimal column density distribution for each transition. The MgII, CIV, and OVI AOD distributions were computed using the doublet. For the CIV $\lambda 1548$ line, we masked out pixels that were unusable as indicated by the two spikes in the sigma spectrum visible in Figure 2. Note the difference in the optical depth as a function of velocity of each transition, especially between MgII and CIV. We also employed the AOD method to compute the remaining column densities presented in Table 1.

Even though the Lyman series is saturated, we have optimally combined all the series lines to produce the H_I column density distribution presented in Figure 4. Note that some central pixels are saturated and we therefore can not obtain a total column density, however, we can compute the H_I column density over a range of velocity windows where there is no saturation.

3.3 Curve of Growth Analysis

We use the curve of growth analysis (COG) to determine the column density limits of various transitions of silicon and for MgII, MgI and CII redward of the galaxy systemic velocity. The equivalent width limits quoted in Table 1 are 3σ limits for a unresolved single cloud. The single cloud assumption for silicon is motivated by the SiII $\lambda 1527$ absorption-line, given that we would likely expect

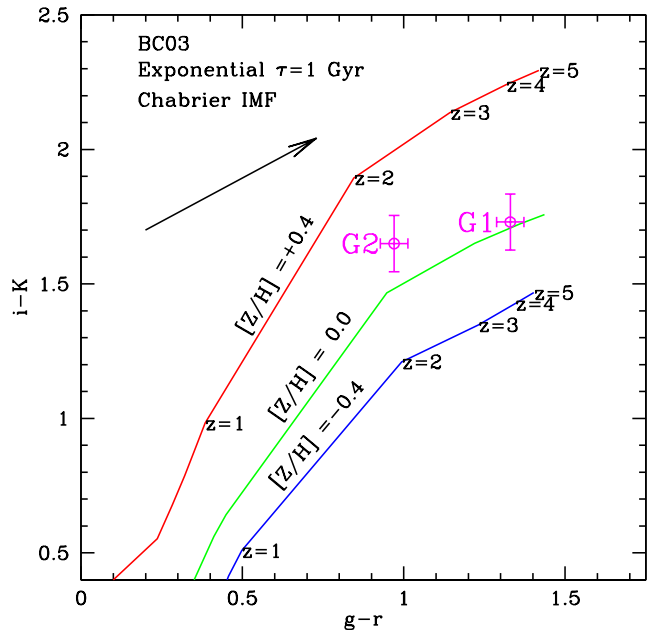


Figure 5. — Color-color diagram for $g - r$ versus $i - K$. Lines are Bruzual & Charlot (2003) stellar population models for an exponential star formation history and a Chabrier (2003) initial mass function. Stellar metallicities and formation redshifts are also labeled. The points (magenta) are galaxies G1 and G2, where G2 is the focus of this paper and discussions of G1 can be found in a companion paper Churchill et al. (2012b). A reddening vector for $E(B - V) = 0.1$ at the rest-frame of the galaxies is provided for reference. G2 is consistent with stellar population model of solar metallicity.

to detect the remaining silicon transition as a single cloud component consistent with the strongest MgII cloud located at roughly -180 km s^{-1} .

The measured equivalent width limits are small and being on the linear part of the curve of growth implies that the column densities are mostly independent of the Doppler parameter (b). In fact, for $b \geq 5$, the predicted column density are independent of b . We find that the SiII column density is best constrained by the SiII $\lambda 2515$ data and the SiIV column density is best constrained by the SiIV $\lambda 1394$ data.

There also exists *HST*/FOS spectra of this quasar that covers additional silicon transitions, among other metal-lines, however, we find that the equivalent widths were inconsistent with the predictions by the COG analysis; this was not the case for the STIS or COS data. We note that the FOS measurements published in Jannuzi et al. (1998); Churchill et al. (2000a) are plagued by unresolved blends from the other H_I lines and therefore we do not use the FOS data in our analysis.

It is important to state that although the curve of growth analysis seems to systematically underestimate the column densities of the metal-lines (Prochaska 2006), the silicon transitions do not provide sufficient constraints on our analysis and do not affect our results. We provide these column density measurements for completeness.

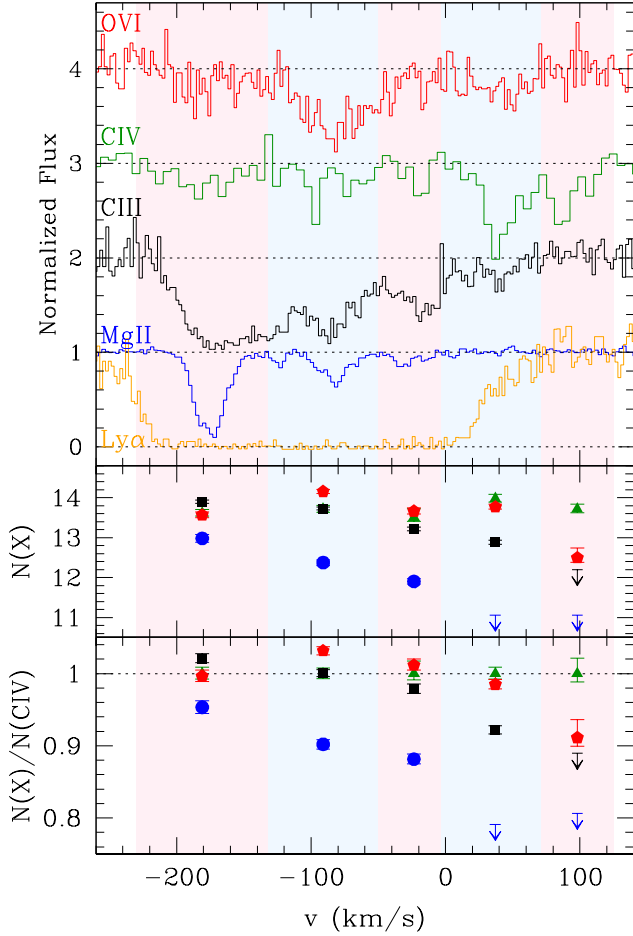


Figure 6. — (top) Overlay of the $\text{Ly}\alpha$, $\text{MgII } \lambda 2796$, $\text{CIII } \lambda 1777$, $\text{CIV } \lambda 1551$ and $\text{OVI } \lambda 1032$ transitions. Note that the low ionization $\text{MgII } \lambda 2796$, $\text{CIII } \lambda 1777$ trace the bulk of the hydrogen while the higher ionization states trace both low and high hydrogen column densities. The line morphologies of CIV and OVI are quite different to those of MgII and CIII . — (middle) AOD column densities of MgII (blue circles), CIII (black squares), CIV (green triangles) and OVI (red pentagons) as a function of different velocity bins. The data points are located in the center of the bin, while the shading indicates the full velocity width of the bin. — (bottom) Same as above except the values are normalized to $N(\text{CIV})$. Note that CIV and OVI have similar behavior blueward of the systemic velocity.

4 RESULTS: GALAXY PROPERTIES

In Figure 1 we present a $g'r'Ks$ color composite centered on the quasar with galaxies G1 and G2 labeled. We find that G2 tends to be bluer than G1, which likely indicates a younger stellar population. This is coincident with the fact that G1 exhibits weak (3 \AA) $[\text{OII}]$ emission.

In Figure 5, the $g-r$ versus $i-K$ colors of G1 and G2 are compared to the Bruzual & Charlot (2003) stellar population models obtained using EzGal (Mancone & Gonzalez 2012) for an exponential star formation history, with an e -folding time of 1 Gyr, and a Chabrier (2003) initial mass function. The K-band is crucial in breaking degeneracies between other star formation history models since it is very sensitive to the old stellar populations. We tested a variety of models and find that anything but a prolonged $\tau = 1$ Gyr exponential model do not fit the data.

In our companion paper Churchill et al. (2012b) we discuss G1, although we note that G1 is redder, formed at an earlier epoch

and is more massive. The model comparison suggests that G2 is dominated by a ~ 4 Gyr stellar population with slightly greater than solar metallicity abundance and formed at redshift $z \sim 2$. We also note while G2 has an $[\text{OII}]$ rest equivalent width of 3.0 \AA , it is consistent with galaxies having $U-B \gtrsim 1.0$ (Cooper et al. 2006): red galaxies with little-to-no star formation. Thus, the stellar population of G2 should be dominated by an older population as the model suggests. Adopting the K -band mass-to-light ratio associated with this stellar population model, we estimate the total stellar mass of G2 to be $M_* \sim 1 \times 10^{11} M_\odot$.

We further estimate the halo virial mass from the stellar mass using GalMass (Stewart 2011). GalMass uses abundance matching models from Moster et al. (2010) along with semi-empirical fits to observed galaxy gas fractions to convert between the stellar and gas mass described in (Stewart et al. 2009). There is roughly a 0.25 dex uncertainty in M_{vir} at a fixed M_* due to the systematics in estimates of M_* (Behroozi, Conroy, & Wechsler 2010). The mean galaxy gas and baryonic masses are also estimated from Stewart et al. (2011a) who employed the baryonic Tully-Fisher relation (McGaugh 2005), the stellar, gas, and dynamical mass relation (Erb et al. 2006), and galaxy-gas fraction and stellar mass relation (Stewart et al. 2009). We estimate the halo virial mass, gas mass and baryonic mass to be $\log M_{\text{vir}} = 12.9$, $\log M_{\text{gas}} = 10.1$ $\log M_b = 11.1$, respectively.

5 RESULTS: ABSORPTION

From Figure 2 and Figure 4, it is clear that the absorption properties vary significantly as a function of ionization level. In Figure 6, we overlay selected transitions to further demonstrate this. It is clear that MgII and CIII (along with SiII and MgI) have similar kinematics and trace the bulk of the hydrogen. While CIV and OVI trace some of the same gas, their kinematics and their relative absorption strengths differ. Furthermore, they both exist where there are diffuse hydrogen column densities and no MgII absorption.

In the bottom panels of Figure 6 we show the AOD column densities as a function of the velocity for each transition. Note that the OVI follows similar abundances to CIV across the profile, while MgII and CIII differ and decrease toward the positive velocities. It appears quite clear that the kinematics and the abundance patterns show that CIV and OVI trace different phases of gas and this difference become greater redward of the galaxy systemic velocity where the hydrogen column density decreases by 2 dex.

Given the observed kinematic and abundance profile differences, we have broken the absorption regions into two separate components and model them independently. In Table 1, we list the total column densities for gas blueward, $N(X)^{\text{blue}}$, and redward, $N(X)^{\text{red}}$, of the galaxy systemic velocity. In the following subsections, we present models to explain the observed absorption kinematics and also apply photo+collisional ionization models to determine the origins and the physical properties of the gas.

5.1 Kinematic Models

Steidel et al. (2002) obtained the rotation curve for G2 and is represented in Figure 7. Note that all of the MgII , and the majority of the CIII , resides to one side of the galaxy systemic velocity. Churchill & Steidel (2003) noted that the CIV , and here we see the OVI , resides on both sides of the galaxy systemic velocity.

To explore the origins of the MgII absorption, Steidel et al. (2002) employed a simple lagging halo model that extended the galaxy rotation velocity out into a co-rotating gaseous disk/halo.

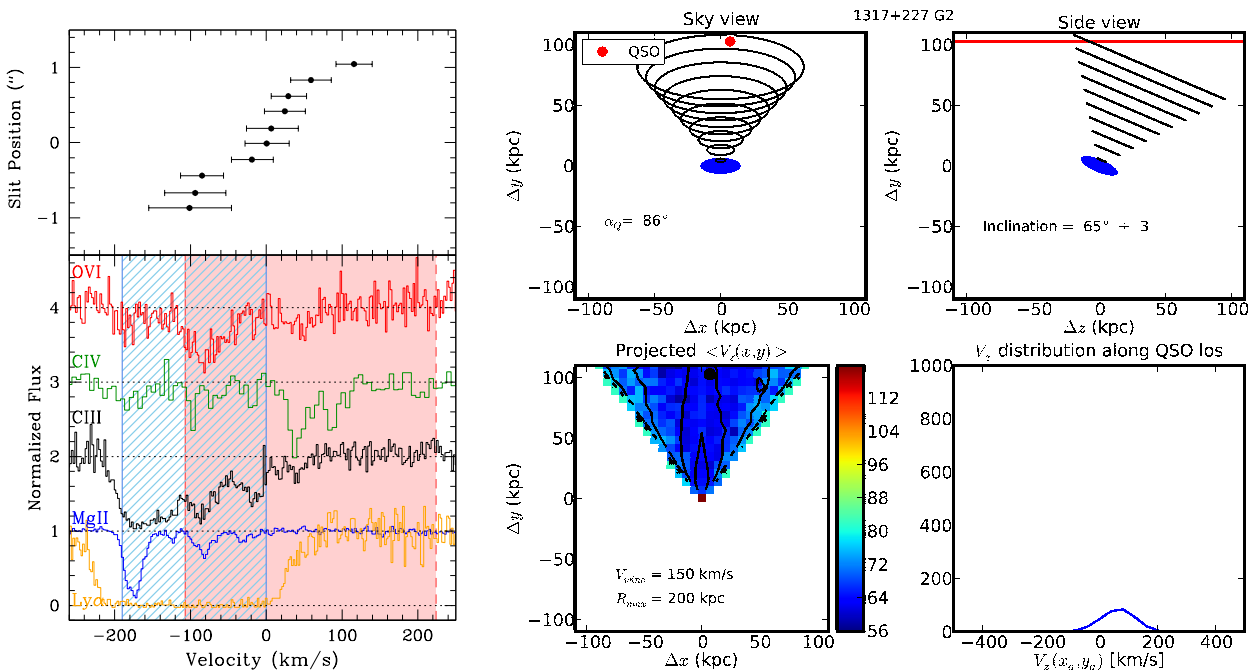


Figure 7. — (left) The data points show the rotation curve of G2 obtained from Steidel et al. (2002). Below are a selection of absorption transitions where the hashed region (blue) shows the rotating thick disk modeled velocities, while the solid shading (red) indicates the wind model velocity predictions. Note that all of the MgII, and the majority of the CIII, resides to one side of the galaxy systemic velocity while CIV, and some OVI and CIII also resides redward of the galaxy systemic velocity. — (right) The wind model of Bouché et al. (2011) applied to G2. — (top-left panel) The wind modeled cone, having an opening angle of 30 degrees, viewed face-on where the galaxy is represented as the filled ellipse and with the QSO line-of-sight marked. — (top-right panel) A side view. — (bottom-left panel) The average cloud line-of-sight velocities as a function of position within the wind. The QSO location is represented as the filled circle. — (bottom-right panel) The line-of-sight velocity distribution of the clouds at the location of the quasar. We find that an outflow velocity of 150 km s^{-1} produces a good match to the data and comparable to the results found by Bouché et al. (2011). Note the peak of the density distribution coincides with the bulk of the CIV absorption.

They determined that a lagging halo model can account all of MgII absorbing gas kinematics, even though the absorption occurs at $D = 103.9$ kpc. The predicted model velocities are highlighted by the hashed (blue) region below the galaxy rotation curve in Figure 7. Further note that the observed rotation curve does not go deep enough to reach the flat part of the curve. This implies there is additional/higher galaxy kinematics that were not included in the model, thus the vertical solid (blue) line on the left of the absorption profiles would move towards bluer velocities. It is quite clear that the low ionization gas seems coupled to the disk kinematics similar to the models of Stewart et al. (2011b). However, the observed co-rotating MgII absorption extends to larger D than the models of Stewart et al. (2011b) since, at $z = 1.4$, their simulated disks extend only to ~ 40 kpc. Thus, it remains unclear if there is size evolution as a function of redshift or if the simulations (without metals) properly trace the metal-lines or if this is a result of simulating only a few galaxies. Aside from these caveats, the similarities between the observations and the simulations are suggestive that this absorption system exhibits signatures of cold mode accretion.

Note that the rotating disk model does not account for all of the absorption. Perhaps that given that the quasar line-of-sight passes along the minor axis of the galaxy and that G2 is undergoing some star-formation (indicated by the [OII] emission shown in Figure 1), then it is possible that some of the absorption arises from outflows.

By analyzing 10 $z \sim 0.1$ MgII absorbers selected from

Kacprzak et al. (2011a), Bouché et al. (2011) found a bi-modal distribution of the azimuthal orientation of the quasar sight-lines: half of the sight-lines aligned with the major axis and half within $\alpha = 30$ degree of the minor axis. The bi-modal azimuthal angle distribution was later confirmed by Kacprzak et al. (2012) using a sample of 88 absorption-selected galaxies ($W_r(2796) \geq 0.1 \text{ \AA}$) and 35 non-absorbing galaxies ($W_r(2796) < 0.1 \text{ \AA}$). These results indicate that both gaseous disks and strong bipolar outflows could contribute to MgII cross-section. Bouché et al. (2011) also applied a simple bi-conical wind model that was able to reproduce the observed MgII kinematics for the sight-lines aligned with the minor axis. We apply their model here in an effort to reproduce the observed absorption kinematics. Their galactic wind model consists of 10^5 “clouds” moving at a constant velocity (V_{out}) that is determined from the absorption data. The clouds are contained within a cone that has a 30 degree opening angle.

Figure 7 shows the wind model for G2 using the orientation parameters from Kacprzak et al. (2011b). The top-left panel shows the cone view face-on and the top-right panel shows a side view of the cone, where the galaxy is represented as the filled ellipse and with the QSO line-of-sight marked. The bottom-left panel shows the average cloud line-of-sight velocities a function of position. The bottom-right panel shows the distribution of the cloud line-of-sight velocities along the quasar sightline. The wind speed is tuned to match the observed velocity range. For this particular case, we find that an outflow velocity of 150 km s^{-1} produces a good match to

the data and are comparable to the results found by Bouché et al. (2011).

In the lower-right panel, we see the predicted absorption distribution peaks at roughly 50 km s^{-1} , where the majority of the C IV and some O VI resides. The wind model velocity range is also shown as the solid shaded region over the absorption profiles. The model could also account for the observed C IV and O VI blueward of the galaxy systemic velocity, although the model predicts only predicts of few percent of the gas is expected at these velocities.

If the opening angle or the wind speed is increased, the model velocity range would also increase and could include all of the observed absorption. However, increasing these parameters will not reproduce the observed optical depth distribution of the cold and hot gas. While our current model is tuned to reproduce the absorption reward of the galaxy systemic, a different model would not be able to predict the strong absorption residing at -200 km s^{-1} . A model with increased opening angle and/or wind speed would also predict additional absorption beyond $+200 \text{ km s}^{-1}$ where none is observed. Therefore, it is very difficult to reproduce both the velocity and optical depth distributions of the cold and hot gas using only the wind model.

The wind model can not account for the bulk of the Mg II, Mg I, Si II and C III. Thus, although the galaxy is forming stars, winds are likely not responsible for the cool gas, but could be responsible for the hot gas. One would naively expect that the infalling gas would be metal poor while the outflowing gas to be metal enriched. We explore the gas-phase metallicities in the next subsections in order to determine the possible origins of the absorption.

5.2 Cold Gas Phase

To determine the physical properties of the cool gas blueward of the galaxy systemic velocity, we use Cloudy (Ferland et al. 1998) to model the ionization conditions. We follow the standard assumption of a photoionized uniform slab of gas that is in ionization equilibrium and is illuminated with a Haardt & Madau (2011) ionizing spectrum, where the UV photons arise from quasars and galaxies. The ionization parameters, U , and the metallicity of the gas are varied to match the observations of $N(X)^{\text{blue}}$ in Table 1 (column 6).

In Figure 8 we show the model results computed for $\log[N(\text{H I})] = 18.3 \pm 0.3$ and a metallicity $[X/H] = -1.67$. We find a narrow range of ionization parameters that reproduce the cool gas phase. The thin curves show the models while the thicker curves show the model values permitted by the data. The C III provides the tightest constraints on the ionization parameter of $-3.25 \leq \log U \leq -3.21$. Less stringent constraints are also found from Si II and Mg II yields $-3.38 \leq \log U \leq -3.16$.

In Figure 8, the same Cloudy models are shown as a function of U and metallicity. The constraints placed on U and the models confine the allowed range of metallicity. The C III measurements limit the metallicity to $-1.68 \leq [X/H] \leq -1.64$. Recall that the C III column density measurement blueward of the galaxy systemic velocity is the unblended portion of this transition. If we were to include the small contribution of the C III redward of the galaxy systemic velocity our results would still be consistent. The Si II and Mg II yields a less stringent of $-1.73 \leq [X/H] \leq -1.63$. Thus, this cool gas component has low metallicity and a low ionization parameter.

In summary, the C III column density provides the tightest constraint and yields a $\log U = -3.23 \pm 0.2$ and $[X/H] = -1.66 \pm 0.02$. The gas is primarily ionized since the ionization fraction $X(\text{H I}) = N(\text{H I})/N(\text{H}) = 0.088 \pm 0.002$ with a hydrogen number den-

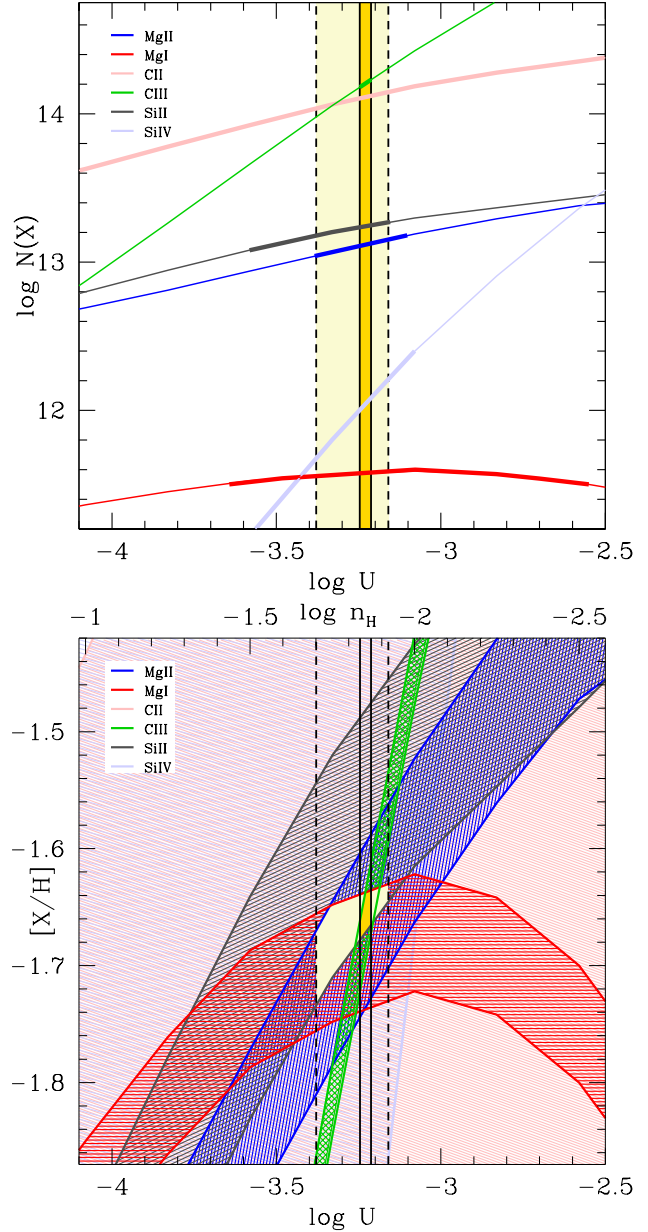


Figure 8. — (top) The Cloudy predicted column densities, as a function of the ionization parameter, for a metallicity of $[X/H] = -1.67$ and a $\log[N(\text{H I})]=18.3$. The bold portions of the curves show the observed column densities, $N(X)^{\text{blue}}$, blueward of the galaxy systemic velocity (Table 1 column 6). The vertical lines show the ionization parameter constraints provided by the data. The C III provides the tightest constraints of $-3.25 \leq \log U \leq -3.21$ indicated between the solid vertical lines (gold region). Si II and Mg II provide secondary constraints of $-3.38 \leq \log U \leq -3.16$ as noted by the vertical dashed lines (yellow region). — (bottom) The ionization parameter as a function of metallicity for the above model. The shaded regions show the model ranges due to the measurement errors in $N(X)^{\text{blue}}$. The vertical lines are the ionization parameter constraints provided by the top panel and provides the region of acceptable metallicities. The overlapping shaded regions of each ion within the constraints provided by U have a solid shading and outlines the allowed metallicities of this cold gas. Again, C III places the tightest constraints on the metallicity $-1.68 \leq [X/H] \leq -1.64$. Thus, the cool gas has low metallicity and a low ionization parameter.

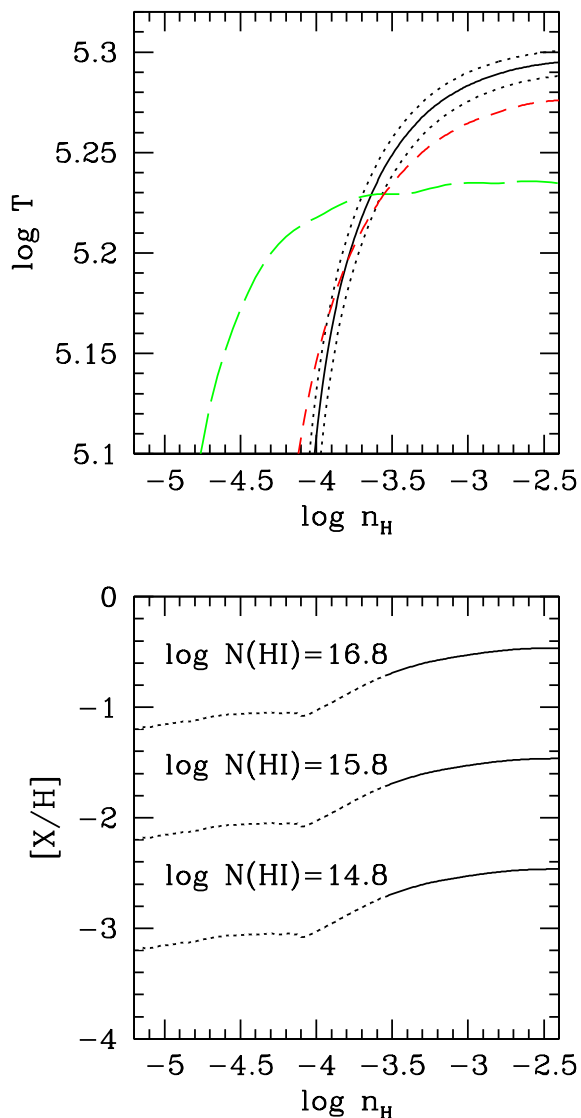


Figure 9. — (top) The photo+collisional ionization models (Churchill & Klimek 2012) as a function of temperature and hydrogen density. The lines indicate abundance ratios which are independent of the hydrogen column density. The solid line is the C IV/O VI column density ratio along with its measured error (dotted lines). The long and short dashed lines are the C III/C IV and C III/O VI column density ratio, respectively. The C III/C IV and C III/O VI dashed curves are lower limits on the allowed temperature range for a given hydrogen density. Note that full self consistency is when the dashed curves to fall below the black curve. The gas has a hydrogen density of $\log n_H > -3.5$ and the C IV/O VI provides a temperature constraint of $\log T = 5.23 - 5.29$. — (bottom) The metallicity as a function of hydrogen density for various hydrogen column densities. We provide conservative limit of $\log N(\text{HI}) < 16.8$ [see text] which yields $[X/H] < -0.5$.

sity of $\log(n_H) = -1.85 \pm 0.02$. The physical size of the cloud is $L = N_H/n_H = 521 \pm 2$ pc.

Note that C IV and O VI do not appear on these plots. The column densities predict for this photo-ionized modeled gas would be $\log N(\text{C IV}) = 11.88 - 11.94$ and $\log N(\text{O VI}) = 7.29 - 7.35$. This predicted column densities are no where near the measured values of $\log N(\text{C IV}) = 14.11$ and $\log N(\text{O VI}) = 14.33$. Thus, it is likely that

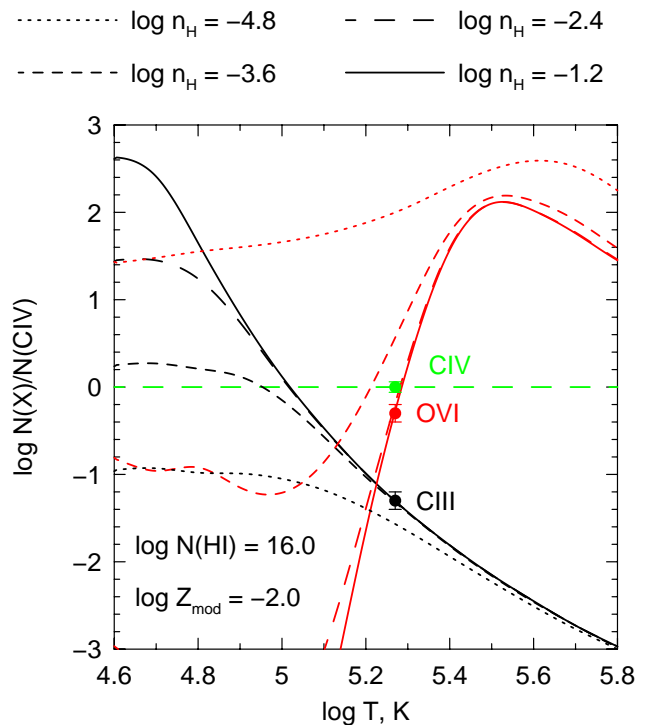


Figure 10. — The photo+collisional ionization models obtained from Churchill & Klimek (2012) as a function of temperature and column density normalized to $N(\text{C IV})$. The data points are the AOD measured column densities of absorption redward of G2’s systemic velocity, $N(x)^{\text{red}}$, shown in Table 1 (column 8). We allowed the gas temperature and metallicity to vary for a range of hydrogen densities, n_H . The data constrain the gas temperature to be 185,000K and limits $\log n_H \geq -2.4$. In Figure 11 we provide the constraints on the warm phase metallicity.

these ions are not part of the cool gas phase and are likely part of a separate “warm/hot” collisional ionized gas phase. In Figure 6, note that the C IV and O VI have different kinematics that the lower ionization species further indicated that the absorption blueward of the galaxy systemic velocity is probing two gas phases. In the next section we model the warm gas.

5.3 Warm Gas Phase

We employed our own photo+collisional ionization code (Churchill & Klimek 2012) to model the warm gas phase since it is optimally designed for optically thin gas with no ionization structure. In short, the code incorporates photoionization, Auger ionization, direct collisional ionization, excitation-autoionization, photo-recombination, high/low temperature dielectronic recombination, charge transfer ionization by H^+ , and charge transfer recombination by H^0 and He^0 . All metal transitions and ionization stages for elements up to zinc are modeled. Solar abundance mass fractions are obtained from Draine (2011) and Asplund et al. (2009) and a Haardt & Madau (2011) ionizing spectrum is used for the ultraviolet background. The model inputs are the hydrogen number density (n_H), kinetic temperature and the gas metallicity while the model outputs are the electron density, and the ionization and recombination rate coefficients, ionization fractions and the number densities for all ionic species. Our models are consistent with those of Cloudy for $\log(n_H) > -3.75$. For $\log(n_H) < -3.75$,

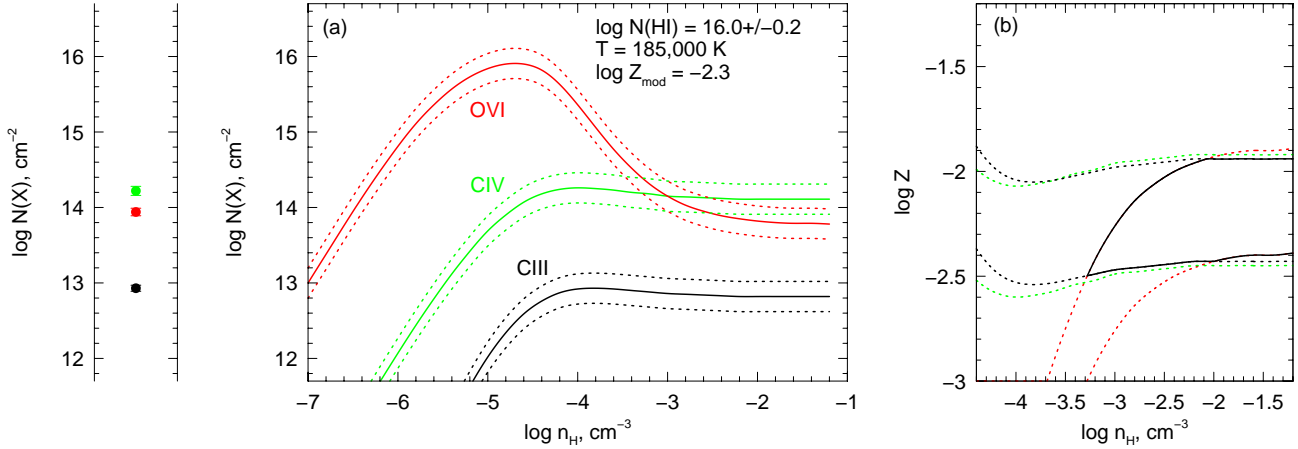


Figure 11. — (left) The data points are the AOD measured column densities of absorption redward of G2’s systemic velocity, $N(x)^{\text{red}}$, shown in Table 1 (column 8). — (middle) The photo+collisional ionization models obtained from Churchill & Klimek (2012) for C III, CIV and OVI using a fixed temperature of 185,000 K and $[X/H] = -2.3$. The spread in the models is due to the error in the measured H I column density of $\log[N(\text{H I})]=16.03\pm 0.18$ (dotted lines). — (right) The allowed metallicity and n_{H} for the model on the left. While n_{H} is not well constrained, we find $-2.50 \leq [X/H] \leq -1.93$ and $\log n_{\text{H}} > -3.3$ for the lower metallicity limit and $\log n_{\text{H}} > -2.1$ for the upper metallicity limit.

cosmic ray heating in Cloudy tends to yield over-ionized clouds with large sizes (< 100 kpc). When cosmic ray heating is turned off, Cloudy has convergence issues and tends to produce ratios of column densities for adjacent species that do not follow a trend physical with ionization potential. We have reconciled these issues in our models and a detailed comparison will be presented in Churchill & Klimek (2012).

5.3.1 Warm Gas Phase Blueward of Systemic Velocity

In modeling the cold gas phase we noted that we are unable to account for the measured $\log N(\text{CIV})=14.11$ and the $\log N(\text{OVI})=14.33$. Thus, these ions are not part of the cool gas phase and are likely part of a separate warm collisionally ionized gas phase. Here we model the diffuse warm gas found blueward of G2’s systemic velocity. Furthermore, all of the measured C III is well modeled as being associated with the cool gas phase, however, there could possibly exist a small fraction of a measurable warm C III component hidden. If we assume that the warm component is within the 0.2 dex measurement error of C III, then there can be at most $\log N(\text{C III}) < 12.87$ in the warm phase.

In Figure 9 we show column density ratios, which is independent of $N(\text{H I})$, as a function of temperature and hydrogen density. The solid line is the CIV/OVI column density ratio along with its measured error (dotted lines). The long and short dashed lines are the C III/CIV and C III/OVI column density ratios, respectfully. The dashed curves are lower limits on the allowed temperature range for a given hydrogen density since $\log N(\text{C III}) < 12.87$. Note that full self consistency is when the dashed curves fall below the solid curve. The models indicated that the gas has a hydrogen density of $\log n_{\text{H}} > -3.5$ and the CIV/OVI provides temperature constraints of $\log T = 5.23 - 5.29$, where the exact temperature is dependent on n_{H} .

In Figure 9, we also show the gas metallicity as a function of $N(\text{H I})$ and n_{H} . We are unable to measure the H I column density associated with this warm component. However, Churchill et al. (2007) states that if an additional hydrogen component having $\log N(\text{H I}) > 16.8$ was added to the total hydrogen column density,

then it would measurably modify the shape of the Lyman limit. Thus, this provides a conservative estimate of the additional $N(\text{H I})$ that could be associated with the warm component since we assume it can not contribute to the Lyman limit. The column density limits provides a metallicity limit of $[X/H] \lesssim -0.5$. Note that the metallicity scales with hydrogen column density by the same amount. It is likely that the metallicity is much lower, though we can not provide any further constraints.

5.3.2 Warm Gas Phase Redward of Systemic Velocity

Here we model the diffuse warm gas found redward of G2’s systemic velocity. We allowed the gas temperature, the gas metallicity and the hydrogen density to vary to match the column density measurements, $N(X)^{\text{red}}$, from Table 1 (column 8). We only detect C III, CIV and OVI redward of the galaxy systemic velocity. The H I associated with the warm gas phase was computed from the AOD H I column density redward of the galaxy systemic velocity. As shown in Figure 4, the H I absorption profile is not saturated redward of the galaxy systemic velocity and contains a $\log N(\text{H I})=16.03\pm 0.18$.

Figure 10 shows the models column densities normalized to that of CIV. The data are well constrained with the warm phase gas having a temperature of $T = 185,000 \text{ K}$ while there seems to be a larger range in the hydrogen density such that $\log n_{\text{H}} \geq -2.4$ for a fixed metallicity. In order to accurately determine the range of metallicities and n_{H} , we show the predicted column densities and metallicities as a function of n_{H} in Figure 11. Again, the measured (left) and modeled (middle) column densities are shown. The model spread, indicated by the dotted lines, is dominated by the error in the measured H I column density. We find that the models do not well constrain the n_{H} but provide reasonable constraints on the metallicity. We find $-2.50 \leq [X/H] \leq -1.93$ and $\log n_{\text{H}} > -3.3$ for the lower metallicity limit and $\log n_{\text{H}} > -2.1$ for the upper metallicity limit.

Table 2. Modeled Absorbing Gas Properties

Name	velocity [km s ⁻¹]	logN(HI)	log(T)	log(U)	log(n_{H})	[X/H]
cold	$-240 \leq v_{\text{abs}} \leq -3$	18.3 ± 0.3	$3.82 - 5.23$	$-3.25 \leq \log(U) \leq -3.21$	$-1.87 \leq \log(n_{\text{H}}) \leq -1.83$	$-1.68 \leq [X/H] \leq -1.64$
warm blue	$-240 \leq v_{\text{abs}} \leq -3$	$< 16.8^a$	$5.23 - 5.29$	$\log(U) \geq -3.5$	$\log(n_{\text{H}}) > -3.5$	$[X/H] \leq -0.5^a$
warm red	$-3 \leq v_{\text{abs}} \leq 220$	16.0 ± 0.18	5.27	$\log(U) \geq -3.3$	$\log(n_{\text{H}}) > -3.3$	$-2.50 \leq [X/H] \leq -1.93$

^a See text in Section 5.3.1 for a discussion of the $N(\text{H I})$ upper limit used and how that affects the absorption metallicity.

6 DISCUSSION

The galaxy G2 has a stellar metallicity greater than solar, yet it contains $[X/H] \sim -2$ halo gas detected in absorption at 104 kpc from the galaxy center. The data likely suggests that the absorbing gas is tracing cold accretion. A summary of the absorption gas properties is presented in Table 2. The kinematic differences⁴ seen between the high and low ionization states, as shown in Figure 6, and the photo+collisional ionization models suggest that the absorption is multi-phase. This may imply that the warm and cold gas physically arises in different locations or that the absorbing gas is not well mixed.

The quasar sight-line probes absorption within three degrees of the projected minor axis of G2 (Kacprzak et al. 2011b), which is a location recently interpreted to be favorable for probing galactic-scale winds (Bouché et al. 2011; Bordoloi et al. 2011; Kacprzak et al. 2012). G2 is dominated by a relatively old stellar population, yet it has measurable [O II] emission (3.0 Å) and thus is likely undergoing some current star-formation that could possibly produce winds.

In Figure 7 we show a wind model that can account for the bulk of the warm gas kinematics, both redward and blueward of G2's systemic velocity, yet it does not reproduce the kinematics of the cold gas. This might imply that some of the warm gas could originate from winds, however, the 2 – 2.5 order of magnitude difference between the galaxy stellar metallicity and the absorption metallicity is inconsistent with a wind model (e.g., Oppenheimer et al. 2010). Assuming a constant wind speed of 150 km s⁻¹, as suggested by the models, the absorbing gas would have left the galaxy 670 Myr ago. Given such a short time scale, G2 still expected to have solar metallicity at that epoch according to mass-gas metallicity relations (e.g., Savaglio et al. 2005) and simulations (e.g., Oppenheimer et al. 2010). The recycling for wind material is less than 1 Gyr (Oppenheimer et al. 2010), thus, if the gas were wind material and was well mixed, it would be expected to have a metallicity similar to that of the parent stellar population. However, the efficiency at which the gas is mixed within the halo environment is still unclear. (Sijacki et al. 2011) shows that poor gas mixing in simulations may be an artifact the suppression of dynamical fluid instabilities demonstrated by comparing smooth particle hydrodynamics codes to that of the moving mesh code AREPO. However, some LLSs exhibit metallicity variations across the absorption profile (e.g., Prochter et al. 2010). Thus, if the gas probed by this absorption system is poorly mixed, it is plausible that the gas is entrained in a outflowing wind (see Alūzas et al. 2012; Schaye et al. 2007). Although, the current observational evidence suggests that Mg II entrained in outflowing material may,

on average, have a maximum projected extension of ~ 50 kpc. (Bordoloi et al. 2011). Thus, the combination of the low metallicity, the relative kinematics between the galaxy and the absorbing gas, and the large projected distance between the gas and the galaxy, corroborate an accretion scenario.

In summary, although the kinematic model works well for the warm gas, it is inconsistent with the expected outflow metallicities and this gas would have already been recycled several times and should have near solar metallicity. This leads to the idea that this meal poor gas could be infalling towards the galaxy.

Galaxy G2 has a stellar mass of $M_* = 1 \times 10^{11} M_{\odot}$ and a viral mass of $M_{\text{vir}} = 8 \times 10^{12} M_{\odot}$. Cold mode accretion is less favored for galaxies with $M_{\text{vir}} \gtrsim 10^{12} M_{\odot}$ since the cold gas can become shock-heated as it enters the halo and hot mode accretion becomes the dominant mode of accretion (e.g. Dekel & Birnboim 2006; Kereš et al. 2009; Stewart et al. 2011a,b; van de Voort et al. 2011; van de Voort & Schaye 2011). For massive galaxies, infalling gas can be shock heated to temperatures above 10^6 K, however, accretion via dense filaments can be maintained past the shock regions, although have dramatically decreased covering fractions compared to low mass galaxies, and still accret onto the galaxy (e.g. Kereš et al. 2009; Stewart et al. 2011a,b; Faucher-Giguère et al. 2011; van de Voort et al. 2011; van de Voort & Schaye 2011). The hot gas pressure compresses cold streams and provides an efficient means of bringing cold pristine gas to the host galaxy and should be traced by LLS (e.g., Fumagalli et al. 2011). A $\log N(\text{H I}) = 18.3$ corresponds to $\Delta\rho/\rho > 1000$ at $z \leq 1$ (e.g., Davé et al. 1999) indicates that these high densities could make its way into the galaxy center.

Although massive galaxy halos are built up from hot accretion, comprising of 80 – 90% of the total accretion, it becomes less important for accretion on to the ISM [50 – 70% hot mode] (van de Voort et al. 2011). However, van de Voort et al. (2011) states that the cold gas accreting onto the ISM in massive galaxies increases with increasing simulation resolution. This could arise since gas clouds could be easily disrupted in SPH simulations, and the cold fraction would increase if higher densities were reached in higher resolution simulations. A lower hot fraction of gas accreted onto the galaxy occurs because the hot gas temperature increases with the viral temperature, or halo mass, resulting in longer cooling times (e.g., Wiersma et al. 2009) and yielding less hot gas cooling to ISM temperatures. However these results could also be dependent on the type of simulations used (Sijacki et al. 2011).

Using the cosmological formulae for virial quantities of Bryan & Norman (1998), we derived the radius, $R_{\text{vir}} = 380$ kpc, the circular velocity $v_{\text{circ}} = 280$ km s⁻¹ and the temperature, $T_{\text{vir}} = 3 \times 10^6$ K. The quasar is probing along the minor axis of the galaxy within the viral radius at $R/R_{\text{vir}} \sim 0.3$, well within the shock radius. Furthermore, the halo gas is expected to be heated to the viral temperature. The temperatures deduced from our models for the warm gas phase is 1.8×10^5 K for gas blueward of the systemic velocity

⁴ Ding, Charlton, & Churchill (2005) modeled the C IV and lower ionization states of Mg II, Mg I and Fe II with the same kinematic structure. It is clear from the fit residuals that the kinematics are not well modeled with similar velocity structure although they do have some similarities.

and 1.9×10^5 K for the gas redward of the galaxy systemic velocity: both are an order of magnitude cooler than that of the virial temperature. However, this gas can possibly cool after it had been shocked, although as mentioned above, the cooling time for hot shock-heated gas is much longer for massive galaxies.

We can estimate a cool gas phase temperature by using the Doppler parameters derived from Mg II absorption (Kacprzak et al. 2011b). The Mg II Doppler parameters range from $2.1 - 10.8$ km s⁻¹ and if we assume that all the broadening is thermal, we can compute upper limits on the temperature of $6.6 \times 10^3 - 1.7 \times 10^5$ K. These temperatures are upper limits since some of the line-broadening could be due to turbulence, and the Voigt profiles fits to the data assume a minimum number of “clouds”; if more clouds were inserted, than the velocity width of each line would decrease. Thus, the cold gas has temperatures well expected for cold mode accretion and not post-shock heated cooling gas accreting within a virial radius ratio of 0.3 (van de Voort & Schaye 2011).

The absorption kinematics also hints to an origin of cold-mode accretion. The metal poor cold-phase, and redward warm-phase, has kinematics consistent with extended disk rotation (Kacprzak et al. 2010a; Steidel et al. 2002). This result has been interpreted using cosmological simulations to be a signature of cold gas accreting via filaments that drive the angular momentum of the galaxy, thereby mimicking its rotation out at larger impact parameters (Kacprzak et al. 2010a; Stewart et al. 2011b). This is consistent with van de Voort & Schaye (2011) that shows cold accretion gas having a higher radial velocities and scales with increases mass compared to the flat radial velocity distribution of the hot-mode accretion as a function of mass.

As we previously mentioned, the metallicities of the warm ($[X/H] = -2$ to -2.5) and cold ($[X/H] = -1.7$) gas are low and appear to be consistent with metallicities expected for cold-mode accretion at $R/R_{\text{vir}} \sim 0.3$ (van de Voort & Schaye 2011) and do not mimic the metallicities expected for the ISM, the hot halo, and the host galaxy (Oppenheimer et al. 2010). The temperatures and kinematics of the absorbing gas is also consistent with what is expected for cold-mode accretion. Thus, it is likely that the absorption is probing cold pristine gas infalling towards the center of the disk, further fueling star formation.

7 CONCLUSIONS

In this paper, we present detailed photo+collisional ionization models and kinematics models of the multi-phase absorbing gas, detected within the *HST/COS*, *HST/STIS*, and Keck/HIRES spectra of the background quasar TON 153, associated with star-forming spiral galaxy at $z = 0.6610$. The sightline probes the projected minor axis of the galaxy at projected distance of 0.3 virial radii, well inside the virial shock radius predicted for a galaxy of this mass, implying that if the gas is infalling that it is post shock heated accretion or a cold filament. We obtained followup *HST/COS* data to study other metal-lines in order to determine the halo gas properties and their origins. This galaxy was targeted as a candidate cold accretion probe supported by kinematic and orientation results presented by Steidel et al. (2002); Kacprzak et al. (2010a, 2011b).

Our main results can be summarized as follows:

(i) From *g'r'i'Ks* photometry and stellar population models, we determined that G2 is dominated by a ~ 4 Gyr stellar population with slightly greater than solar metallicity abundance and formed at redshift $z \sim 2$. We estimate an $M_* = 1 \times 10^{11} M_{\odot}$ implying an $\log M_{\text{vir}} = 12.9$.

(ii) The low ionization states, Mg I, Si II, Mg II and C III, have similar absorption kinematics, abundance ratios across the profile, and trace the bulk of the hydrogen, while C IV and O VI trace some of the same gas, their kinematics, abundance ratios, and their relative absorption strengths differ. We infer that the low and high ionization states trace different gas phases.

(iii) Modeling the cold gas blueward of G2’s systemic velocity, $N(X)^{\text{blue}}$, we constrain $\log T = 3.82 - 5.23$, $-3.25 \leq \log(U) \leq -3.21$, $-1.87 \leq \log(n_{\text{H}}) \leq -1.83$, and $-1.68 \leq [X/H] \leq -1.64$. The gas is cold and very metal poor: consistent with cold accretion. We are unable to account for the measured $N(\text{C IV})$ and $N(\text{O VI})$ when modeling the cold phase, thus, these ions are likely part of a separate warm collisionally ionized gas phase.

(iv) A lagging halo model can account for all of low ionization absorption, hinting that this gas is coupled to the disk and simulations interpret this as a detection cold mode accretion.

(v) Modeling the warm gas blueward of G2’s systemic velocity, $N(X)^{\text{blue}}$, we find $n_{\text{H}} > -3.5$ and $\log T = 5.23 - 5.29$. Armed with only a conservative limit of hydrogen column density that could be associated with the warm component [$N(\text{H I}) > 16.8$], we estimate $[X/H] \lesssim -0.5$, although it is highly likely that the metallicity is much lower.

(vi) Modeling the warm gas redward of G2’s systemic velocity, $N(X)^{\text{red}}$, we find hot and metal poor gas with $T = 185,000$ K, $-2.50 \leq [X/H] \leq -1.93$ and $n_{\text{H}} > -3.3$.

(vii) The quasar line-of-sight passes along G2’s minor axis and a wind model can account for the observed C IV and O VI redward and blueward of the galaxy systemic velocity. However, given the 2 – 2.5 order of magnitude difference between the galaxy stellar metallicity and the absorption metallicity demonstrates the gas can not arise from galactic winds.

It remains plausible that this low metallicity gas arises from unidentified satellites around the host galaxy or from the incomplete mixing between metal enriched and metal poor halo gas. However, the combination of the relative kinematics, temperatures, and relative metallicities allows us to conclude that the multi-phase gas detected in absorption likely arises from cold accretion around this massive galaxy. For high mass galaxies the cold accretion cross-section is expected to be a few percent, so our absorption system and others cited in the literature could be a by-chance low probability intersection of a filament, or the resolution effects in the simulations (see van de Voort & Schaye 2011) are underestimating the covering fraction of cold flows. This system also contradicts current results that predict that all absorption detected in quasars probing gas along the projected minor axis of galaxies is produced by winds (Bordoloi et al. 2011; Bouché et al. 2011; Kacprzak et al. 2012): This is clearly not the case here.

ACKNOWLEDGMENTS

We thank Nicolas Bouché for his useful comments, models and for carefully reading this paper. We also thank the anonymous referee for carefully reading the manuscript and for providing insightful comments. CWC was partially support through grant HST-GO-11667.01-A provided by NASA via the Space Telescope Science Institute, which is operated by the Association of Universities for Research in Astronomy, Inc., under NASA contract NAS 5-26555. CWC thanks GGK, and Michael T. Murphy, and Swinburne Faculty Research Grants for providing funding for a visit to Swinburne University of Technology. Based on observations made with the NASA/ESA *Hubble Space Telescope* (PID 11667), and obtained

from the Hubble Legacy Archive, which is a collaboration between the Space Telescope Science Institute (STScI/NASA), the Space Telescope European Coordinating Facility (ST-ECF/ESA) and the Canadian Astronomy Data Centre (CADC/NRC/CSA). Some of the data presented herein were obtained at the W.M. Keck Observatory, which is operated as a scientific partnership among the California Institute of Technology, the University of California and the National Aeronautics and Space Administration. The Observatory was made possible by the generous financial support of the W.M. Keck Foundation. This work is also based on observations obtained with the Apache Point Observatory 3.5-meter telescope, which is owned and operated by the Astrophysical Research Consortium. Observations were also made with the NASA/ESA *Hubble Space Telescope*, or obtained from the data archive at the Space Telescope Institute.

REFERENCES

- Alúzar, R., Pittard, J. M., Hartquist, T. W., Falle, S. A. E. G., & Langton, R. 2012, arXiv:1206.6037
- Asplund, M., Grevesse, N., Sauval, A. J., & Scott, P. 2009, *ARA&A*, 47, 481
- Bahcall, J. N., Bergeron, J., Boksenberg, A., et al. 1993, *ApJS*, 87, 1
- Bahcall, J. N., Bergeron, J., Boksenberg, A., et al. 1996, *ApJ*, 457, 19
- Barlow, R. 2003, arXiv:physics/0306138
- Behroozi, P. S., Conroy, C., & Wechsler, R. H. 2010, *ApJ*, 717, 379
- Bertin, E., & Arnouts, S. 1996, *A&AS*, 117, 393
- Bordoloi, R., Lilly, S. J., Knobel, C., et al. 2011, arXiv:1106.0616
- Bouché, N., Hohensee, W., Vargas, R., Kacprzak, G. G., Martin, C. L., Cooke, J., & Churchill, C. W. 2012, arXiv:1110.5877
- Brooks, A. M., Governato, F., Quinn, T., Brook, C. B., & Wadsley, J. 2009, *ApJ*, 694, 396
- Bruzual, G., & Charlot, S. 2003, *MNRAS*, 344, 1000
- Bryan, G. L., & Norman, M. L. 1998, *ApJ*, 495, 80
- Ceverino, D., Dekel, A., & Bournaud, F. 2010, *MNRAS*, 404, 2151
- Chabrier, G. 2003, *PASP*, 115, 763
- Chen, H.-W., Helsby, J. E., Gauthier, J.-R., Shectman, S. A., Thompson, I. B., & Tinker, J. L. 2010a, *ApJ*, 714, 1521
- Chen, H.-W., Kennicutt, R. C., Jr., & Rauch, M. 2005, *ApJ*, 620, 703
- Chen, H.-W., Lanzetta, K. M., & Webb, J. K. 2001, *ApJ*, 556, 158
- Churchill, C. W., & Klimek, E. S. 2012, *PASP*, in prep
- Churchill, C. W., Kacprzak, G. G., Steidel, C. C., et al. 2012b, arXiv:1205.0595
- Churchill, C. W., Kacprzak, G. G., & Steidel, C. C. 2005, in *Probing Galaxies through Quasar Absorption Lines*, IAU 199 Proceedings, eds. P. R. Williams, C.-G. Shu, & B. Ménard (Cambridge: Cambridge University Press), p. 24
- Churchill, C. W., Kacprzak, G. G., Nielsen, N. M., Steidel, C. C., & Murphy, M. T. 2012a, *ApJ*, submitted
- Churchill, C. W., Kacprzak, G. G., Steidel, C. C. & Evans, J. L. 2007, *ApJ*, 661, 714
- Churchill, C. W., Mellon, R. R., Charlton, J. C., Jannuzi, B. T., Kirhakos, S., Steidel, C. C., & Schneider, D. P. 2000a, *ApJS*, 130, 91
- Churchill, C. W., Rigby, J. R., Charlton, J. C., & Vogt, S. S. 1999, *ApJS*, 120, 51
- Churchill, C., & Steidel, C. 2003, *The IGM/Galaxy Connection. The Distribution of Baryons at $z=0$* , 281, 149
- Churchill, C. W., & Vogt, S. S. 2001, *AJ*, 122, 679
- Churchill, C. W., Vogt, S. S., & Charlton, J. C. 2003, *AJ*, 125, 98
- Coil, A. L., Weiner, B. J., Holz, D. E., et al. 2011, *ApJ*, 743, 46
- Cooksey, K. L., Prochaska, J. X., Chen, H.-W., Mulchaey, J. S., & Weiner, B. J. 2008, *ApJ*, 676, 262
- Cooper, M. C., Newman, J. A., Croton, D. J., et al. 2006, *MNRAS*, 370, 198
- D'Agonstini, G. 2000, arXiv:physics/0403086
- D'Agonstini, G., & Raso, M. 2000, arXiv:physics/0002056
- Davé, R., Hernquist, L., Katz, N., & Weinberg, D. H. 1999, *ApJ*, 511, 521
- Dekel, A., & Birnboim, Y. 2006, *MNRAS*, 368, 2
- Dekel, A., Birnboim, Y., Engel, G., et al. 2009, *Nature*, 457, 451
- Ding, J., Charlton, J. C., & Churchill, C. W. 2005, *ApJ*, 621, 615
- Dixon, W. V., et al. 2010, *Cosmic Origins Spectrograph Instrument Handbook, Version 3.0* (Baltimore: STScI)
- Draine, B. T. 2011, *Physics of the Interstellar and Intergalactic Medium*, Princeton University Press, ISBN: 978-0-691-12214-4 (Table 1.4, p8)
- Erb, D. K., Steidel, C. C., Shapley, A. E., Pettini, M., Reddy, N. A., & Adelberger, K. L. 2006, *ApJ*, 646, 107
- Faucher-Giguère, C.-A., Kereš, D., & Ma, C.-P. 2011, *MNRAS*, 417, 2982
- Ferland, G. J., Korista, K. T., Verner, D. A., et al. 1998, *PASP*, 110, 761
- Fumagalli, M., Prochaska, J. X., Kasen, D., et al. 2011, *MNRAS*, 418, 1796
- Haardt, F., & Madau, P. 2011, *ApJ*, arXiv:1105.2039
- Jannuzi, B. T., Bahcall, J. N., Bergeron, J., et al. 1998, *ApJS*, 118, 1
- Kacprzak, G. G., & Churchill, C. W. 2011, *ApJ*, 743, L34
- Kacprzak, G. G., Churchill, C. W., & Nielsen, N. M. 2012, arXiv:1205.0245
- Kacprzak, G. G., Churchill, C. W., Barton, E. J., & Cooke, J. 2011a, *ApJ*, 733, 105
- Kacprzak, G. G., Churchill, C. W., Ceverino, D., Steidel, C. C., Klypin, A., & Murphy, M. T. 2010a, *ApJ*, 711, 533
- Kacprzak, G. G., Churchill, C. W., Evans, J. L., Murphy, M. T., & Steidel, C. C. 2011b, *MNRAS*, 416, 3118
- Kacprzak, G. G., Murphy, M. T., & Churchill, C. W. 2010, *MNRAS*, 406, 445
- Kacprzak, G. G., Churchill, C. W., Steidel, C. C., & Murphy, M. T. 2008, *AJ*, 135, 922
- Kereš, D., Katz, N., Fardal, M., Davé, R., & Weinberg, D. H. 2009, *MNRAS*, 395, 160
- Kereš, D., Katz, N., Weinberg, D. H., & Davé, R. 2005, *MNRAS*, 363, 2
- Kriss, G. A., *COS Instrument Handbook 2011-01*, (Baltimore, STScI)
- Mancone, C. L., & Gonzalez, A. H. 2012, *PASP*, 124, 606
- Martin, C. L., & Bouché, N. 2009, *ApJ*, 703, 1394
- Martin, C. L., Shapley, A. E., Coil, A. L., et al. 2012, arXiv:1206.5552
- McGaugh, S. S. 2005, *ApJ*, 632, 859
- Moster, B. P., Somerville, R. S., Maulbetsch, C., et al. 2010, *ApJ*, 710, 903
- Nestor, D. B., Johnson, B. D., Wild, V., et al. 2011, *MNRAS*, 412, 1559
- Noterdaeme, P., Srianand, R., & Mohan, V. 2010, *MNRAS*, 403, 906

- Ocvirk, P., Pichon, C., & Teyssier, R. 2008, *MNRAS*, 390, 1326
- Oppenheimer, B. D., Davé, R., Kereš, D., et al. 2010, *MNRAS*, 406, 2325
- Péroux, C., Bouché, N., Kulkarni, V. P., York, D. G., & Vladilo, G. 2011, *MNRAS*, 410, 2237
- Prochaska, J. X. 2006, *ApJ*, 650, 272
- Prochter, G. E., Prochaska, J. X., O'Meara, J. M., Burles, S., & Bernstein, R. A. 2010, *ApJ*, 708, 1221
- Rao, S. M., Turnshek, D. A., & Nestor, D. B. 2006, *ApJ*, 636, 610
- Ribaudo, J., Lehner, N., Howk, J. C., et al. 2011, *ApJ*, 743, 207
- Rigby, J. R., Charlton, J. C., & Churchill, C. W. 2002, *ApJ*, 565, 743
- Rubin, K. H. R., Weiner, B. J., Koo, D. C., et al. 2010, *ApJ*, 719, 1503
- Rubin, K. H. R., Prochaska, J. X., Koo, D. C., & Phillips, A. C. 2011, arXiv:1110.0837
- Savage, B. D., & Sembach, K. R. 1991, *ApJ*, 379, 245
- Savaglio, S., Glazebrook, K., Le Borgne, D., et al. 2005, *ApJ*, 635, 260
- Schaye, J., Carswell, R. F., & Kim, T.-S. 2007, *MNRAS*, 379, 1169
- Schlegel, D. J., Finkbeiner, D. P., & Davis, M. 1998, *ApJ*, 500, 525
- Sijacki, D., Vogelsberger, M., Keres, D., Springel, V., & Hernquist, L. 2011, arXiv:1109.3468
- Simard, L., Willmer, C. N. A., Vogt, N. P., Sarajedini, V. L., Philips, A. C., Weiner, B. J., Koo, D. C., Im, M., Illingworth, G. D., & Faber, S. M. 2002, *ApJS*, 142, 1
- Skrutskie, M. F., Cutri, R. M., Stiening, R., et al. 2006, *AJ*, 131, 1163
- Steidel, C. C., Erb, D. K., Shapley, A. E., et al. 2010, *ApJ*, 717, 289
- Steidel, C. C., Kollmeier, J. A., Shapely, A. E., Churchill, C. W., Dickinson, M., & Pettini, M. 2002, *ApJ*, 570, 526
- Steidel, C. C., Dickinson, M., & Persson, S. E. 1994, *ApJ*, 437, L75
- Steidel, C. C., & Sargent, W. L. W. 1992, *ApJs*, 80, 1
- Stewart, K. R. 2011, arXiv:1109.3207
- Stewart, K. R., Bullock, J. S., Wechsler, R. H., & Maller, A. H. 2009, *ApJ*, 702, 307
- Stewart, K. R., Kaufmann, T., Bullock, J. S., et al. 2011a, *ApJ*, 735, L1
- Stewart, K. R., Kaufmann, T., Bullock, J. S., et al. 2011b, *ApJ*, 738, 39
- Thom, C., Werk, J. K., Tumlinson, J., et al. 2011, *ApJ*, 736, 1
- Tremonti, C. A., Moustakas, J., & Diamond-Stanic, A. M. 2007, *ApJL*, 663, L77
- Tripp, T. M., Jenkins, E. B., Bowen, D. V., et al. 2005, *ApJ*, 619, 714
- Tumlinson, J., Thom, C., Werk, J. K., et al. 2011, arXiv:1111.3980
- van de Voort, F., & Schaye, J. 2011, arXiv:1111.5039
- van de Voort, F., Schaye, J., Booth, C. M., Haas, M. R., & Dalla Vecchia, C. 2011, *MNRAS*, 414, 2458
- Weiner, B. J., et al. 2009, *ApJ*, 692, 187
- Wiersma, R. P. C., Schaye, J., & Smith, B. D. 2009, *MNRAS*, 393, 99
- Zonak, S. G., Charlton, J. C., Ding, J., & Churchill, C. W. 2004, *ApJ*, 606, 196
- Zibetti, S., Ménard, B., Nestor, D. B., Quider, A. M., Rao, S. M., & Turnshek, D. A. 2007, *ApJ*, 658, 161